Label-Free Fluorescent Mesoporous Bioglass for Drug Delivery, Optical Triple-mode Imaging, and Photothermal / Photodynamic Synergistic Cancer Therapy

Rajendra K. Singh[1,2,*], Amal George Kurian[1,2], Kapil D. Patel[1,2,3], Nandin Mandakhbayar[1,2], Na-Hyun Lee[1,2], Jung-Hwan Lee[1,2,3,4], Jonathan C. Knowles, and Hae-Won Kim[1,2,3,4*]

[1] Institute of Tissue Regeneration Engineering (ITREN), Dankook University, Cheonan 330-714, Republic of Korea

[2] Department of Nanobiomedical Science & BK21 PLUS NBM Global Research Center for Regenerative Medicine, Dankook University, Cheonan 330-714, Republic of Korea

[3] Biomaterials and Tissue Engineering, UCL Eastman Dental Institute, London WC1X8LD, UK

[4] Department of Biomaterials Science, School of Dentistry, Dankook University, Cheonan 330-714, Republic of Korea

[5] UCL Eastman-Korea Dental Medicine Innovation Centre, Dankook University, Cheonan 31116, Republic of Korea

----

*Corresponding author: Tel: +82 41 550 3081; Fax: +82 41 550 3085;

E-mail: singhiitgphd@gmail.com[*], kimhw@dku.edu[*]

For **: ACS Applied Bio Materials**

ABSTRACT

Nanomaterials combined with phototherapy and multimodal imaging are promising for cancer theranostics. Our aim is to develop fluorescent mesoporous bioglass nanoparticles (fBGn) based on carbon dots (CD) with delivery, triple-mode imaging, and photothermal properties for cancer theranostics. A direct and label-free approach was used to prepare multi-color fluorescent fBGn with 3-aminopropyl triethoxysilane (APTES) as the surface functionalizing agent. The calcination at 400 °C provided fBGn with high fluorescence intensity originating from the CD. In particular, a triple-mode emission (fluorescence imaging (FI), two-photon (TP), and Raman imaging (RI)) was observed which depended on CD nature and surface properties such as surface oxidation edge state, amorphous region, nitrogen passivation of surface state, and crystalline region. The fBGn also exhibited phototherapeutic properties such as photodynamic (PDT) and photothermal (PTT) effects. The antitumor effect of the combined PDT/PTT therapy was significantly higher than that of individual (PDT or PTT) therapy. The fBGn, due to the mesoporous structure, the anticancer drug doxorubicin (DOX) could be loaded and released in a pH-dependent way to show chemotherapy effects on cancer cells. The in vivo imaging and biocompatibility of fBGn were also demonstrated in a nude mouse model. The fBGn, with the combined capacity of anticancer delivery, triple-mode imaging, and PTT/PDT therapy, are considered to be potentially useful for cancer theranostics.

Keywords: Bioactive glass; Carbon dot; Multi-color imaging; Optical imaging; Photothermal therapy; Drug delivery

1. INTRODUCTION

Phototherapy with multimodal imaging has a significant impact on cancer cells [1-3]. It is often considered as a promising strategy in the medical field because of its wider application in tumor therapy due to its benefits of real-time observation of cancer sites and photo-induced destruction of cancer cells [1, 3-5]. Both Photothermal (PTT) and photodynamic (PDT) techniques have better therapeutic efficiency as compared to other techniques of the directed at the same target [6-8]. PTT and PDT therapies function based on the optical absorption of light energy and its conversion to heat energy for hypothermia or production of highly toxic reactive components, such as reactive oxygen species (ROS) to destroy cancer cells [6, 7, 9-11]. Active research focussed on developing photo responsive nanotheranostic biomaterials with concurrent PTT and PDT effects. Recent studies showed that certain nanotheranostic biomaterials such as carbon and metal-based nanomaterials possess both PTT and PDT characteristics [10, 12-18]. Typical carbon nanotheranostic biomaterials such as Carbon Dots (CD), Graphene Oxides (GOs), and Carbon Nanotubes (CNTs) have very strong optical near-infrared (NIR) absorption as well as high phototherapeutic efficiency [10, 12, 19-22].

Fluorescent-based nanotheranostic biomaterials can be useful for real-time imaging and observations during the diagnosing of a cancer site. A number of nanomaterials such as semi-quantum dots, Au-based, CD-based, magnetic-based, etc. have been developed for real-time imaging and phototherapy [13, 23-27]. But the use of these nanomaterials are limited due to the major drawbacks such as toxicity and high synthesis costs. However, carbon dots are a good option for multi-modal imaging agents: for fluorescence imaging (FI), two-photon imaging (TP), and Raman Imaging (RI) as they have specific properties such as lower toxicity, specific tunable surface structure, ease of functionalization, excellent stability against light, tunable absorption-emission spectra, etc. [19, 28-31]. Different techniques to develop CD-based nanomaterials such as chemical, microwave, hydrothermal, ultrasonic, oxygen plasma, and electrochemical are known [32, 33]. But we have utilized a simple sol-gel method using APTES as a surface modifying agent followed by heat treatment. Recently other imaging techniques such as TP spectroscopy with NIR wavelength was utilized for biomedical applications including cell imaging and cancer therapy [21, 34-37]. The rate of penetration of NIR laser light was higher as compared to the visible light due to its high intensity which facilitated the deep-layer tissue penetration. Research on different applications of carbon nanotheranostic biomaterials for TP imaging and theranostics are

still going on [21, 38]. Apart from these spectroscopic techniques based on photon absorption and emission, another technique: Raman spectroscopy, can be utilised and is based on inelastic scattering of photons. Raman spectra are more suitable for long-term analysis compared to fluorescence imaging due to its stability. Carbon-based nanomaterials such as CNT, GO, and CDs shows characteristic peaks in Raman spectra and can be used as non-destructive imaging agents for long term cell imaging [21, 39-42].

Chemotherapy is the leading modality destroy cancer cells, but a significant number of anticancer drugs are hydrophobic and hence have poor water-solubility which can be limiting as they are often administered by the intravenous route [43]. The small size and nonporous nature of CD makes it an inefficient carrier for loading anti-cancerous drugs or other biomolecules for therapeutic purposes. Studies showed that intravenous hydrophobic drugs can be conveniently loaded when using mesoporous nanocarriers due to its good drug holding capacity [44-49]. This approach can improve the efficiency of chemotherapy and leads to fewer side effects systemically. Among a wide variety of silica-based nanomaterials, mesoporous bioglass (BGn) may be a good option for targeted delivery, as it has specific properties such as high surface area, tunable pore size, and good biocompatibility [44, 47, 50]. Bioglasses are based on calcium (Ca) and silica (Si) and they are also used for bone and tissue regeneration [49-51]. BGn has a high surface area and hence a high drug-loading capacity and also can be triggered to release by changes in light, pH, temperature, etc. In this present work, we succeeded in developing CD-based bioglass nanotheranostic carriers for real-time monitoring, targeted delivery, and phototherapy.

Herein, we successfully fabricated calcium and silica-based bioglass nanoparticles (BGn) by sol-gel method with APTES and heat treatment at a specific temperature. After heat treatment, APTES generated CD within the silica networks. Systematic **scheme 1** shows that CD-generated BGn (fBGn) has optical triple-mode bioimaging properties such as FI, TP, and RI along with phototherapeutic properties such as PTT and PDT owing to the presence of the CD nanoparticles. We also reported high drug loading and a pH controlled release mechanism, in-vivo fluorescence imaging, and in-vivo biocompatibility. These optical-based fBGn nanocarriers are promising nanotheranostic biomaterials for the future which can be utilized for phototherapy with multimodal imaging in cancer treatment.
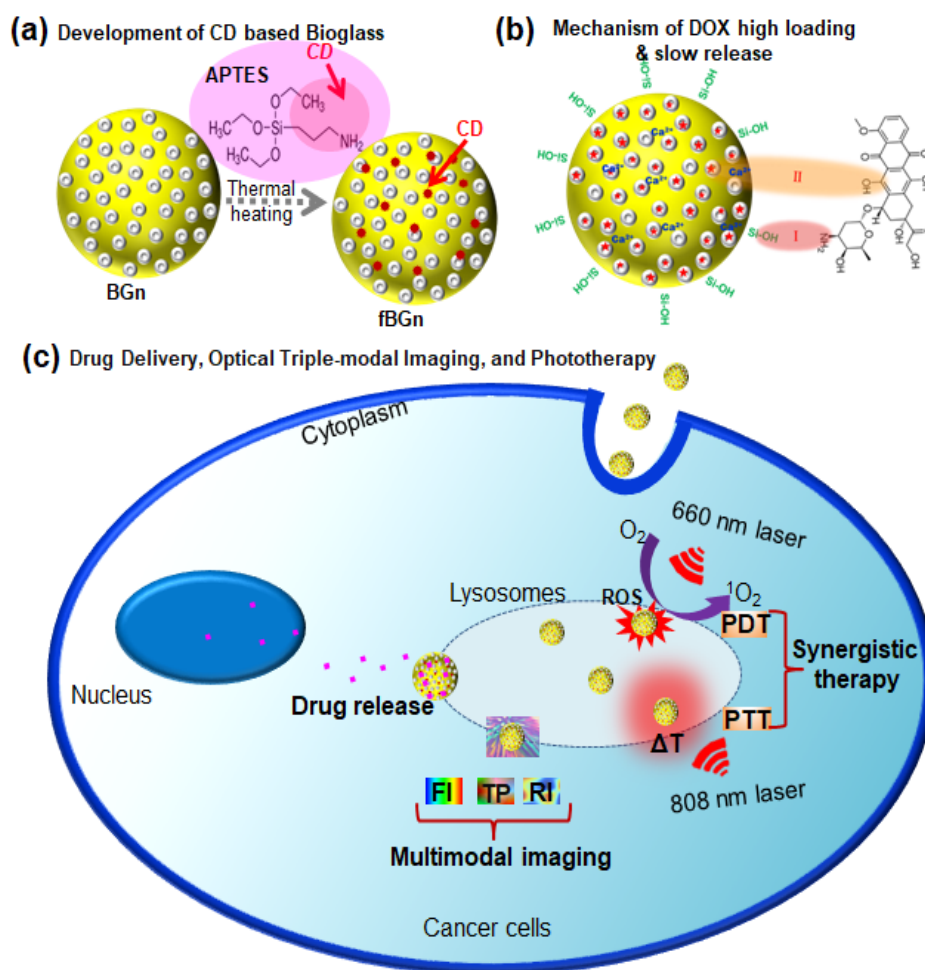
Scheme 1. Schematic representation of (a) development of CD-based bioglass(fBGn), (b) higher DOX loading and controlled release mechanism, and (c) utilized for drug delivery, optical triple-modal imaging, and photo-induced cancer therapy.

2. MATERIALS and METHODS

2.1. Synthesis of fBGn Nanoparticles

Mesoporous bioglass nanoparticles (BGn) were prepared by the Stöber process [52]. 1g Cetyltrimethylammonium bromide (CTAB), 20 mL of 2-methoxyethyl, 10 mL of ethanol, 2 mL of aqueous ammonia was dissolved in 150 mL of distilled water. After 30 min of stirring, $Ca(NO_3)_2 \cdot 4H_2O$, tetraethyl orthosilicate (TEOS) and APTES as a silane functionalizing agent were added into the mixture and stirred for a further 4h. The molar ratio of Ca:Si was about 15:85 and the volume ratio of TEOS to APTES was 1:1. Water and ethanol were used to remove CTAB from the precipitated white powder and finally dried overnight at 70 °C to obtain BGn nanoparticles. The formed BGn nanoparticles were then

heat-treated at different temperatures 250, 300, 350, 400, 450, 500, and 600 °C for 2 h in presence of air and these heat-treated nanoparticles were the end point for fBGn synthesis.

2.2. Sample Characterization

The shape and size of the nanoparticles were confirmed using JEOL-7100 transmission electron microscopy (TEM). Brunauer-Emmett-Teller (BET) surface area, pore-volume, and mesopores size distribution were measured by a surface area analyzer (2SI-MP-9 Quantachome Instruments). The Surface binding chemistry and compositional ratios were analyzed using X-ray photoelectron spectroscopy (XPS). A JES-FA200 electron paramagnetic resonance (EPR) spectrophotometer was used for analyzing the crystal lattice defects present in the nanomaterials. Raman spectra were obtained using a Raman spectrometer (LabRAM HR UV/vis/NIR) operated with 550 nm red light laser. The Chemical bonding structure was then analyzed using Fourier transform infrared spectroscopic technique (FT-IR; Varian 640-IR). Spectra related to optical absorption were obtained using a Cary100 Ultraviolet–visible-near-infrared (UV–vis–NIR) spectrometer. The one-photon excitation fluorescence or fluorescent properties and 2D contour excitation/emission maps of fBGn in aqueous solution were detected using UV–vis filters at various wavelengths using a Jasco FP-6500 device. The decay lifetime was measured using iHR320 spectrophotometer. The two-photon excitation fluorescence spectroscopy of fBGn in aqueous solution was observed using a fiber spectrometer device. An amplified Ti to sapphire laser system with tuning range 550 nm to 900 nm (SpectraPhysics, 50 fs, 1kHz) was used as the light excitation source.

2.3. Confocal Fluorescence Imaging

Glass chamber slides were seeded with HeLa cancer cells (1×10^4 cells) were kept at 37 °C for 12 h. The cell medium was then replaced using fresh cell medium with 50 µg/mL or 100 µg/mL of fBGn nanoparticles and it was then incubated at 37 °C for about 4 h. PBS solution was used for washing the cells and imaged using a confocal microscope having three different excitation wavelengths.

2.4. Raman Imaging

24-well plates were used to culture the cells (1×10^4 cells/well) in α-MEM medium under suitable conditions for culturing and allowed to adhere up to 24h. Cells were then treated with fBGn for about 6 h. After 6h of incubation, the adherent cells were washed using PBS and detached from the plates by

treating it with trypsin–EDTA, and re-suspended with PBS. A drop of cell suspension was added to the silicon wafers to avoid the absorption of fBGn on cell membranes or silicon wafers while using for Raman imaging.

2.5. Evolution of the Photothermal Effect of fBGn

Different concentrations of fBGn (0, 25, 50, 100, 200, and 400 µg/mL) were used for finding the photothermal efficiency induced by laser irradiation 808 nm (1 W/cm^2). The temperature changes of fBGn solution was recorded up to 6 min using a thermal NIR imaging camera. The laser light was switched off after 6 mins and the decrease in temperature was recorded to determine the photothermal efficiency [53, 54].

HeLa cells were utilized for the *in vitro* cytotoxicity studies using a standard CCK-8 method. The cells (1 × 10^4 cells/well) were seeded in a 96-well plate for culturing using α-MEM medium and were allowed to adhere for 24h. These cells were again treated with various concentrations of fBGn (0-800 µg/mL) for about 4 h. Laser irradiation was carried out at 808 nm for 5 min and then incubated for another 24 h. And finally, the relative cytotoxicity of the cells was determined using the standard CCK-8 method.

2.6. Evolution of the Photodynamic Effect of fBGn

1,3-diphenylisobenzofuran (DPBF), a highly reactive trapping agent was used as a standard reagent for the determination of singlet oxygen species ($^1O_2$) in biological systems. In this experiment, fBGn nanoparticles were added to about 1mL of DPBF (100 µg/mL) solution and sonicated for 10 min in the absence of light. This mixture was then irradiated with a 660 nm (80 mW) LED light. The optical absorbance of DPBF (408 nm) was measured at different lengths of time of irradiation using a UV spectrophotometer.

ESR spectral studies were utilized for detecting the $^1O_2$ ROS generated under the influence of irradiated light. 2,2,6,6-Tetramethylpiperidine (TEMP) and 5,5-Dimethyl-1-pyrroline N-oxide (DMPO) were commonly used as $^1O_2$ and $O_2^-\cdot$ (or OH$^-$) trapping agents, respectively. Here, the fBGn solution was added to TEMP or DMPO solution and it was then sonicated in the absence of light for 10 min. The ESR spectra of fBGn sample were measured at room temperature before and after irradiating it using LED light.

ROS Assay Kit was used to confirm the presence of ROS in in-vitro. The cancer cells were seeded in a coverglass chamber for culturing using α-MEM medium for about 24 h. After this, the cells were treated with fBGn for 4h and 2,7-dichloro-dihydro-fluorescein diacetate (DCFH-DA) for another 20 min. Hanks buffered saline solution was used for washing the cells and finally, it was irradiated using 660 nm light for 20 min. After this using a confocal microscope the fluorescence images are obtained.

Cytotoxicity studies of fBGn under *in vitro* conditions was investigated using HeLa cells by following a standard CCK-8 method. Under sterile conditions, the cells were seeded in a 96-well plate (1×10^4 cells/well) using α-MEM medium and allowed to adhere for 24h. These cells were then treated with various concentrations of fBGn ranging from 0 to 800 µg/mL for 4 h. These cells are then irradiated using LED at 660 nm for 20 min and then incubated for another 24 h. Finally, the relative cytotoxicity of cells was determined using the standard CCK-8 method.

2.7. Combined Photothermal and Photodynamic Effects in In-vitro

To study the combination of PDT/PTT efficiency with fBGn, the cells were seeded in a culture plate using α-MEM medium under suitable conditions and the cells are allowed to adhere for about 24h. Cells were treated with fBGn for 4 h and after these cells were treated with 660 nm light for 20 min and 808 nm laser for 5 min respectively. After this treatment, the cells were co-stained using the Live / Dead kit for 20 min and then confocal microscopy was utilized to obtain fluorescence images.

To study the antitumor effects of combined PDT and PTT, the cytotoxicity of fBGn was investigated with HeLa cells in the presence and absence of light. Cells were then treated with fBGn for 4 h followed by exposure to 660 nm light for 20 min and 808 nm laser for 5 min respectively. After incubation, the relative cytotoxicity of the cells were determined using the standard CCK-8 method.

2.8. Anticancer Drug Loading and Release Tests

DOX is a commonly used anticancer drug and for the loading of DOX into MSN or fBGn nanoparticles, 1mg of the nanoparticles were added to 1mL of DOX with different concentrations (80,100, and 120 µg/mL) in the absence of light for 24 h. Then, the solution was centrifuged and absorbance was measured at 484 nm using a UV spectrophotometer. The efficiency of DOX loading was then quantified using a standard spectral curve. In order to study the release curve of DOX from DOX-loaded nanoparticles (MSN and fBGn) two different pH values (5.0 and 7.4) were chosen, with varying time

intervals at 37 °C. The mixture was centrifuged and the supernatant absorbance measured at 484 nm for each time point, and the particles were then resuspended in fresh phosphate buffer at every time point and finally, the DOX release efficiency of the nanoparticles were quantified using the standard curve.

2.9. In-vivo Bioimaging and Biocompatibility

All animal experiments undertaken within the guidelines of the Republic of Korea and the Dankook University Animal Care Committee for Research. In the first experiments, a local injection was carried out, and fBGn nanoparticles (100 µL, 2 mg/mL in saline) were injected into the right area of the body of female nude mice. The fluorescence imaging was then recorded using a Maestro multispectral imaging system. In a second experiment, healthy nude mice was used for in-vivo biocompatibility studies. Different doses of fBGn solution (5, 10, and 20 mg/kg) were injected intravenously via the tail vein in the mouse. In addition, saline was used as a control group. The biocompatibility effects were examined after two weeks, sacrificed and the tissue samples were harvested. The harvested internal organs like heart, lungs, liver, spleen, and kidney were fixed in 4% formaldehyde and then embedded with paraffin and sectioned. This was followed by staining with H&E and then examined using optical microscopy.

3. RESULT and DISCUSSION

3.1. Synthesis of CD Associated fBGn and Its Characterization

Figure 1a is a systematic illustration showing the preparation of the multi-colour fluorescent fBGn. After thermal heating, BGn changed to fluorescent BGn (fBGn) due to the generation of carbon dots (CD) in the matrix. The fBGn was prepared by sol-gel method in the presence of APTES which forms spherical mesoporous silica bioglass (BGn). After thermal treatment, APTES generated CD inside the silica bioglass silica matrix which shows multi-colour fluorescent fBGn. Low and high magnification TEM images of BGn and fBGn with APTES samples are shown in **Figure 1b,** where both spherical BGn and fBGn has a size of 100 ± 10 nm. The fBGn sample had numerous black dots distributed throughout the structure which represent the CD inside the silica matrix. N_2 adsorption/desorption hysteresis loop showed that fBGn have BET surface area of 650 m^2/g, a pore volume of 0.637 cm^3/g, and a pore size of 3.07 nm (**Figure S1**), and this high surface area and mesoporous size is useful for loading biomolecules.
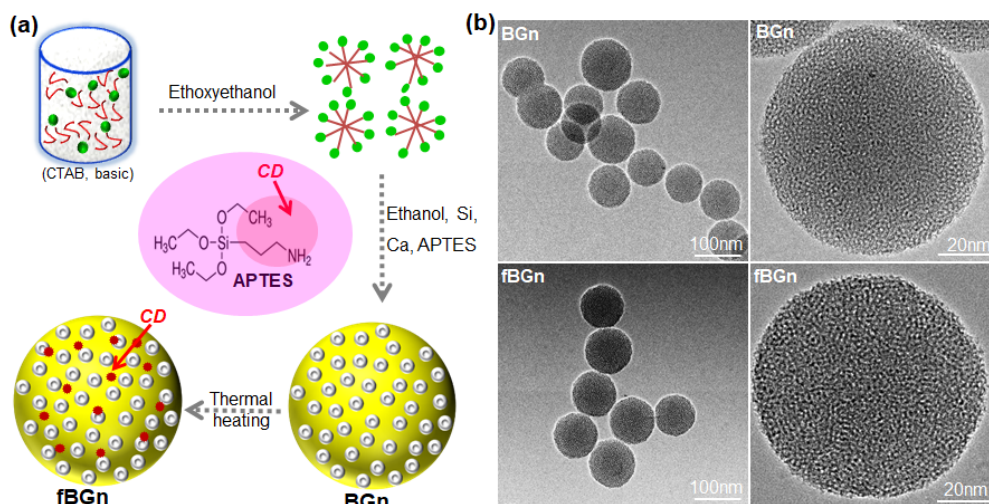
28

Figure 1. (a) Systematic diagram showing the preparation of multi-color fluorescent fBGn. After heat treatment, the formed BGn were fluorescent due to the generation of carbon dots in the matrix. (b) Low and high magnification TEM images of BGn and fBGn samples. fBGn sample shows many black dots distributed throughout the structure.

Next, we confirmed CD properties in fBGn. First, we have analyzed the UV-vis spectra of fBGn samples as shown in **Figure 2a**. The fBGn observed two peaks at ~230 nm and ~340 nm indicating sp^2 domains (C=C bonds) of π–π* electron transition and non-bonding oxygen states (C–O bonds) of n–π* electron transition [55, 56]. Further, the carbon-based nanomaterials have characteristic peaks in the fingerprint region in Raman spectra. The fBGn having two typical Raman peaks as shown in **Figure 2b**, in which D band at ~1400 cm^{-1} and G band at ~1600 cm^{-1} bands are characteristic of the Raman vibration modes sp^3 and sp^2, respectively. The D and G band of the carbon structure either represents disorder or carbon-related defects with amorphous and crystalline nature, respectively [57]. The quality of carbon structure depends on the intensity ratio I_D / I_G [58]. Next, the chemical structure was analyzed using FT-IR spectra in **Figure 2c**. The fBGn showed Si and C related bands which represent Si–O bending (465 cm^{-1}), Si–O–Si symmetric stretching (1095 cm^{-1}), C=C stretching vibration (1414 cm^{-1}), N–H vibration (1560 cm^{-1}), C=O / C=N stretching vibration, and C–O stretching (880 cm^{-1}). The chemical composition, structure, and binding energy were further analyzed using XPS with wide scan which shows the binding energy of Si, Ca, C, N, and O as shown in **Figure 2d**. **Figure 2e** shows the C1$_S$ spectra and these were fitted using the Gaussian method which divided the main peak into four subpeaks: C–C, C–N, C=O, and O–C indicating the graphitic structure of sp^2 bonds. The high-resolution scan, N1$_S$ spectra were deconvoluted into three peaks N-H, (C)$_3$-N, and C-N which indicates that nitrogen is mostly boun to carbon and creates different local energy states with different emission
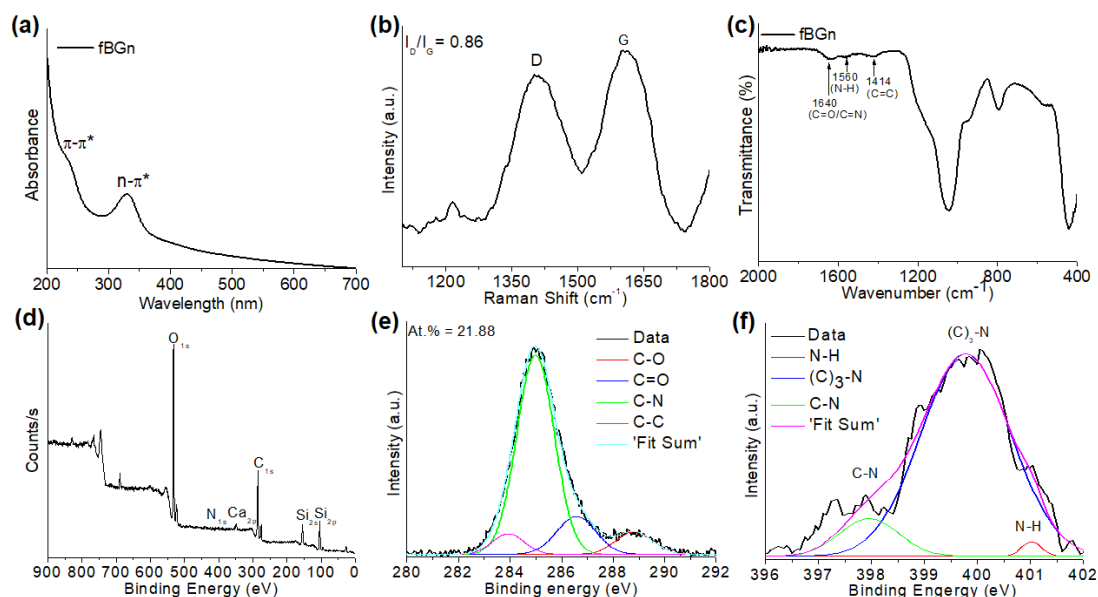
centers (**Figure 2f**).

Figure 2. Characterization of CD associated fBGn: (a) UV-vis spectra, (b) Raman spectra, (c) FT-IR spectra, (d) wide scan XPS spectra, (e) narrow (C1s) scans, and (f) narrow (N1s) scans.

Schematic representation (**Figure 3a**) shows that fBGn sample was treated with 37% hydrofluoric acid (HF) solution to dissolve the silica-based glass and to allow observation of the CDs via TEM. TEM images showed black CD nanoparticles with background decomposition of the bioglass (**Figure 3a**). The size of the CDs was about 1.6 ± 0.4 nm in the inset figure. The high magnification TEM image showed that the CDs had both a crystalline and an amorphous phase [59] which is marked using red and green circles respectively (**Figure 3b**). Further, we investigated the fluorescence properties of fBGn before and after its treatment with HF solution (**Figure 3c**). The intensity of fluorescence was seen to be almost the same before and after HF treatment. This suggests that this strong fluorescence property is due to the CDs and not from the silica matrix. Another possibility for the emission of fluorescence is due to the crystal defects present in the silica matrix. Therefore, we examined the crystal defects present in the materials using EPR spectroscopy to confirm the fluorescence mechanism. EPR spectroscopy is a very sensitive technique used for the confirmation of crystal lattice defects in materials. **Figure 3d** shows that both samples have no EPR signal which indicates materials possess no silica-silica, silica-oxygen, and silica-carbon defects [60, 61]. It also confirmed that the origin of the fluorescence is due to the CD. Based on the above results we proposed the origin of the fluorescence mechanism in **Figure 3e.** CDs show the full range of visible multi-

fluorescence with excitation wavelength-dependent emission. The multicolour fluorescence depends on surface oxidation edge state, amorphous region, nitrogen passivation of the surface state, and crystalline regions [59]. The surface oxidation state is related to carbon and oxygen band which was changed to π or n-domain conjugated electronic transition bandgap. The multi-fluorescent properties are dependent on the surface state energy which mainly depends on C-O, C = O and O = C-OH emission mode. The surface energy state of Nitrogen-containing CDs worked as a passivating agent. This group being an effective agent is used to achieve a passivated state and enabled multi-fluorescence [62, 63].
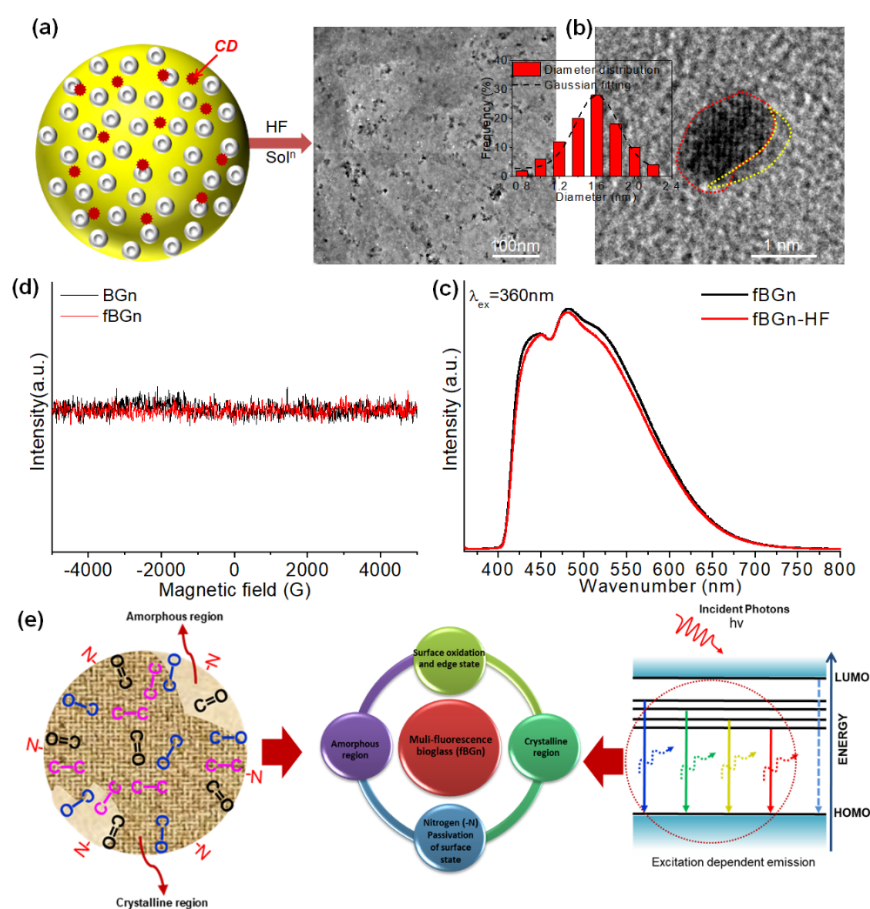

Figure 3. (a) Systematic diagram showing the fBGn samples treated with HF solution and subsequent TEM image. Its shows that CDs as black spots (~1.5 nm) and the background shows that the bioglass was dissolved in HF solution. (b) The high-magnification TEM image shows crystallinity and amorphous nature of CDs. (c) PL emission spectra have a similar intensity of fBGn sample before and after treatment with HF solution. (d) EPR spectra shows no characteristic signal which confirms that the fluorescence is not due to internal defects. (e) schematically illustrated to show the fluorescence mechanism. CDs with different surface states terminated with different groups emits emission dependent on excitation light.

3.2. In-vitro Bioimaging and Multicolour Fluorescence of CD Associated fBGn

Figure 4a is a systematic representation showing the heat-treated BGn at different temperatures ranging from 250 to 600 °C to form CDs inside the silica matrix for multi-color fluorescent fBGn. We investigated the fluorescent properties of fBGn using PL measurement at λ_{ex} 360 nm (**Figure 4b**). The as-prepared sample has no fluorescence property but all heat-treated samples showed PL curve which indicates fluorescence properties. The PL curve showed three emission peaks P_1, P_2, and P_3 which has an emission wavelength in the ranges 428-453 nm, 469-481 nm, and 511-513 nm, respectively (**Figure 4b-c**). The change in emission wavelength depends on the temperature at which fBGn was heated. The maximum peak intensity was observed at 400 °C (**Figure 4d**) due to the maximum generation of CD inside the silica network. After heat treatment at higher temperatures, CD was fully oxidised from the silica matrix. We have carefully chosen a sample at 400 °C for further experiments. The multi-peaks in the curves were fitted by using the Gaussian peak distribution, and the area of the three peaks were calculated using specific wavenumbers (**Figure S2a**). The emission peaks P_1, P_2, and P_3 had areas of 10.04 %, 28.25 %, and 61.71 %, respectively (**Figure S2b**). The area of emission peak P_3 was quite high which represents maximum fluorescence at 512 nm emission wavelength. Next, fBGn was excited at various wavelengths and the intensity of the emission peak was plotted in a 2D contour map as shown in **Figure 4e**. The maximum intensity of emission was observed in the range of 470 to 550 nm. The life-time decay profiles were measured by monitoring the emission at 500 nm using biexponential data and calculated decay time of 6.8 ns (**Figure 4f**). The fBGn nanoparticles were first dispersed in a buffer solution and then excited at different wavelengths using PL spectroscopy. We further observed the full-colour range of fBGn by naked eye with corresponding excitation wavelength using an irradiated Xenon light (**Figure S3**). This fBGn can be utilized for multicolour imaging applications in the biomedical field. This application of fBGn as an effective multicolour imaging agent was successfully demonstrated using cancer cells. First HeLa cancer cells were seeded on cultures plates and then two different concentrations (50 µg mL^{-1} and 100 µg mL^{-1}) of fBGn were treated with cells for about 24 h. After this procedure live cancer cells were observed using CLSM under three different excitation wavelengths blue (405 nm), green (454 nm), and red (546 nm), respectively. We observed the presence of fBGn inside the cytoplasm with different colour emissions. When the concentration of fBGn was increased

then the resultant fluorescence intensities were also increased due to the presence of more fBGn particles. Therefore, this fBGn material can be utilized for multicolour bioimaging in the biomedical field.
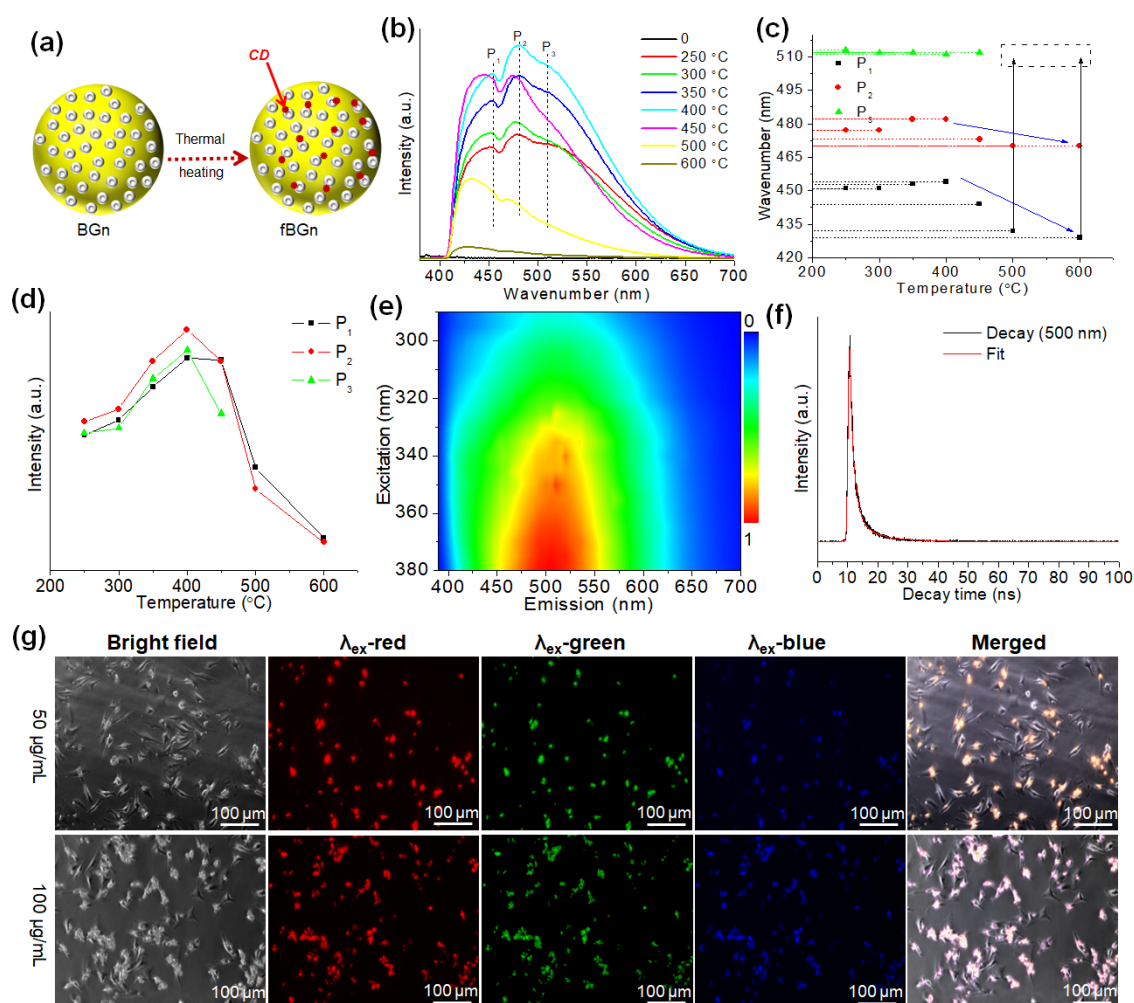

Figure 4. Label-free fluorescence properties of fBGn: (a) Systematic diagram showing the heat-treated BGn samples at different temperatures. During heating, BGn developed fluorescence properties due to the generation of CDs in the matrix. (b) Emission spectra of fBGn with different temperatures at an excitation wavelength of 360 nm. (c) Emission wavenumber and (d) Emission intensity of three peaks (P_1, P_2, and P_3) measured at different temperatures. (e) 2-D excitation-emission contour map of fBGn at different excitation wavelengths. (f) The lifetime decay profiles measured by monitoring the emission at 500 nm with data fitting included. (g) Confocal fluorescence images of two different concentrations of fBGn in live HeLa cells under bright field, corresponding excitation wavelength, and merged images.

3.3. Application of CD Associated fBGn in Two-Photon Spectroscopy for Bioimaging

Another unique property of fBGn was studied using two-photon (TP) fluorescence spectroscopy under NIR wavelength of 800 nm. TP spectroscopy with NIR wavelength is widely used for biomedical applications such as cell imaging and cancer therapy [64-66]. The NIR laser light can easily penetrate deep into the tissues compared to visible light due to its lower absorption properties in soft tissue. The

systematic representation **Figure S4** shows that the fBGn was excited at two different wavelengths (450 and 800 nm) using two different spectroscopic techniques such as one-photon and two-photon spectroscopy. We have observed similar emission trends in both excitation wavelengths. The TP emission spectra of the fBGn at different temperature ranges were studied using an excitation wavelength of 800 nm. The TP emission intensity **Figure 5a** showed that a strong emission peak was observed at ~ 500 nm but the fluorescence intensity depends on the temperature at which fBGn was processed. A higher TP emission intensity of the fBGn sample was observed at 400 °C similar to PL spectroscopy due to the maximum generation of CD inside the silica network. After heat treatment at higher temperatures, CD was fully oxidised from the silica matrix. When the excitation wavelength of laser light was changed from 800 nm to 600 nm, the emission intensity of fBGn at 400 °C was found to decrease with emission peaks at the same position due to the decreased excitation wavelength of laser light **Figure 5b**. We have also analyzed the TP spectral images of fBGn which appeared in green colour on a glass slide (**Figure 5c**). This fBGn system thus demonstrates its future bioapplications in cell imaging, deep tissue imaging, and cancer theranostics by TP spectroscopy.
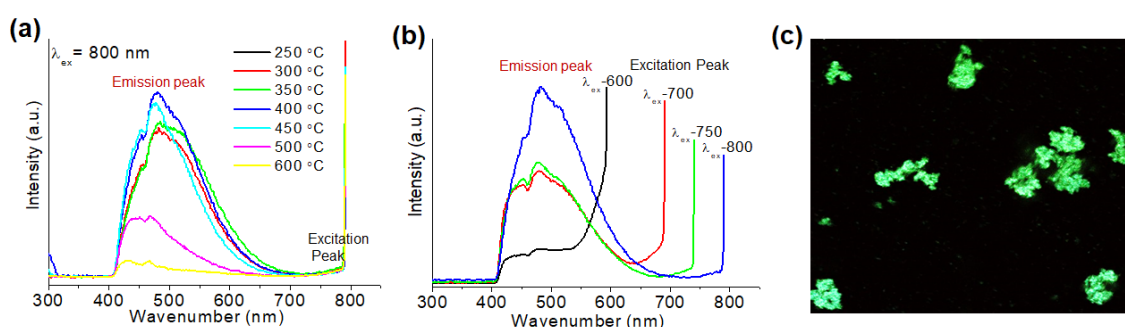

Figure 5. TP spectra of fBGn under excitation with an 800 nm laser light. (a) Emission spectra of fBGn with different temperatures at excitation wavelength 800 nm. (b) Emission spectra of fBGn with different excitation wavelengths. (c) Image of fBGn under excitation with laser light of wavelength 800 nm.

3.4. CD Associated fBGn for Raman Spectroscopy Imaging

Carbon-based nanomaterials are most widely used for cancer theranostics and cell imaging which helps in the detection and diagnosis of diseases. Recent studies showed that techniques such as fluorescence, two-photon, and Raman imaging which displays outstanding spatial resolution can be effectively utilized in cell imaging [21, 40, 41, 67, 68]. Raman imaging is stable for long-term monitoring compared to fluorescence imaging. The carbon-based nanomaterials such as CNT, GO, and CD has a

characteristic fingerprint region in Raman spectra [21, 41]. In the present work, cells were exposed to the fBGn for about 6 h and then harvested. A single drop of cell suspension was placed on a silicon wafer. **Figure 6a** clearly indicates the laser beam and the spherical appearance of the single drop of cells. We used a 514 nm laser beam and fBGn nanoparticles were excited at this wavelength which subsequently showed a red colour in the background due to the characteristic emission. **Figure 6b** shows that these results closely match the PL measurement and confocal image studies. After the removal of the background, fBGn showed a red colour as indicated in **Figure 6c**. We also obtained an optical image of the cell (**Figure 6d**). The BGn having two typical Raman peaks are shown in the inset in **Figure 6e**, in which D (1330 cm^{-1}) and G (1595 cm^{-1}) bands characterize the Raman vibration mode in carbon structures. We used G vibration band as a probe to scan the cells and then the final image represents the Raman image of cells in **Figure 6e**. Significant enhance in Raman signal was observed on increasing the power of laser irradiation, (**Figure 6f**) due to the increase in peak intensity of G band. So, it was inferred that Raman image signals were highly dependent on the intensity of the laser beam and concentration of fBGn. This suggests that fBGn was used for Raman imaging instead of fluorescence imaging of the cells.
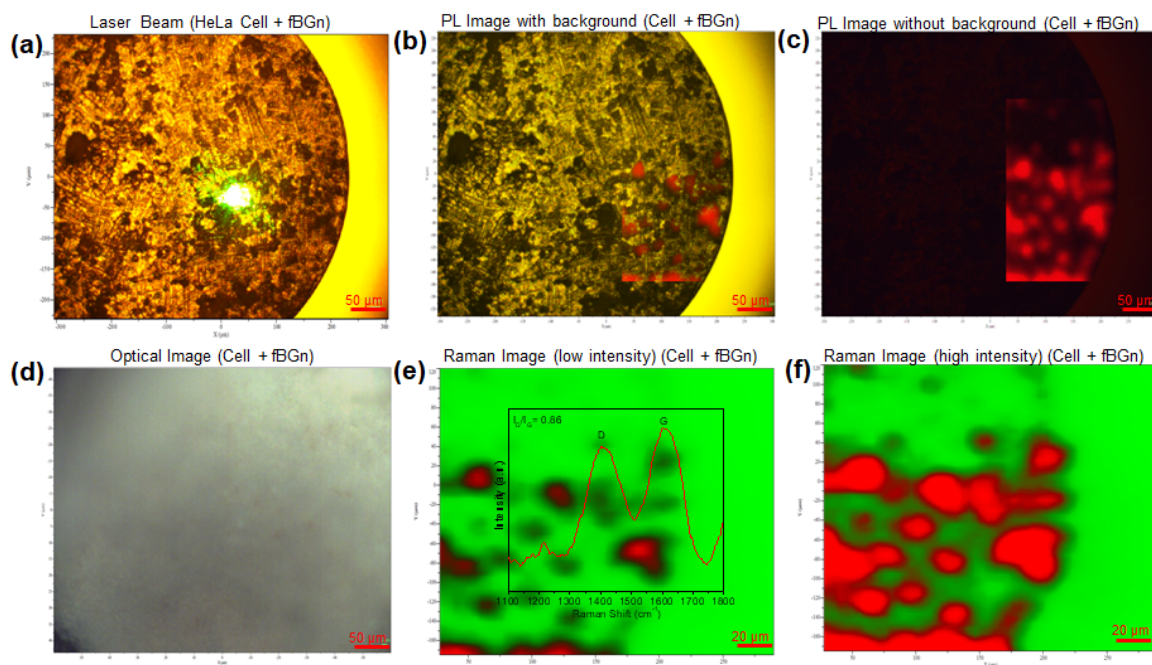

Figure 6. Raman imaging of fBGn with HeLa cells on silica wafers under laser light of wavelength 514nm. (a) Laser spots, (b) PL image with background, (c) PL image without background, (d) Optical image and Raman image of the relative intensity of G with (e) low and (f) high intensity.

3.5. Photothermal and Photodynamic Effects of CD Associated fBGn in Synergistic Cancer Therapy

The photothermal effect is one of the most common properties exhibited by carbon-based nanomaterials [21, 29, 69]. An aqueous solution of fBGn showed different temperatures at different fBGn concentrations when irradiated with laser light (808 nm) up to 600 sec (**Figure 7a**). The temperature of the aqueous solution was increased from 7.6 °C to 38.6 °C at fBGn concentration ranging from 25 μg mL^{-1} to 400 μg mL^{-1}, which is considered signficiant compared to irradiated water with no nanoparticles which showed a $\Delta T \approx 2.4$ °C (**Figure 7b**). Next, the time-dependent temperature curves were recorded until the fBGn aqueous solution reached a stable-state temperature and then cooled down to room temperature (**Figure S5**). Based on heating-cooling data, we used a photothermal conversion formula to calculate the photothermal efficiency [54]. The photothermal efficiency obtained was about 32.4% based on heating-cooling data, which is similar to the previous reports [22]. In addition to this, the NIR images of the aqueous solutions of fBGn were also recorded at different concentrations of fBGn after 600 sec of irradiation using a laser light of wavelength 808 nm (**Figure 7c**). We also quantitatively studied PTT efficiency of fBGn and performed the cytotoxicity studies. As shown in **Figure 7d**, cytotoxicity of HeLa cells decreased with an increase in concentration under irradiation of laser light whereas quantitative PTT efficiency of fBGn is its ability to destroy cancer cells owing to the presence of CDs inside the bioglass. The CDs produced sufficient heat energy to effectively kill the cancer cells under laser light irradiation [70].

We employed ESR spectroscopy to investigate the in vitro PDT ability of fBGn via $^1O_2$ ROS release upon irradiation using LED light (660 nm). The $^1O_2$ or OH$^\cdot$ produced are detected using suitable spin trapping agents TEMPO and BMPO, respectively (**Figure 7e**). As shown in the ESR spectra, TEMPO induced $^1O_2$ signal in fBGn under irradiation of LED light and no $^1O_2$ signal was produced in dark. Therefore, BMPO has not detected any signal because it produced another ROS signal with fBGn. These results show the ability of fBGn to produce $^1O_2$ in the presence of laser light and no other ROS signal was detected. Furthermore, the generation of $^1O_2$ signal by fBGn was confirmed using chemical trapping method, where DPBF a fluorescent molecule was used as trapping agent for absorbing the $^1O_2$ signal. As shown in **Figure 7f**, the absorption intensity of DPBF with fBGn at 408 nm decreased gradually with an increase in the duration of LED light exposure due to the decomposition of DPBF

reacted with $^1O_2$ under light. These results indicate the ability of fBGn to generate $^1O_2$ in the presence of LED light. The rate of $^1O_2$ generation or quantum yields was calculated by linear fitting of the DBPF absorption and the irradiation time (**Figure S6**). The $^1O_2$ quantum yields is 0.86 which is similar to the previous reports [71]. The Moreover, the detection of $^1O_2$ ROS level with fBGn in HeLa cancer cells was analyzed using a ROS assay kit. As shown in **Figure 7g**, the HeLa cells treated with fBGn showed enhanced green fluorescence under LED light. In contrast, in the absence of fBGn no green signal was detected. We have observed green fluorescence in presence of fBGn because fBGn nanoparticles exhibits fluorescence, whereas this fluorescence is not observed uniformly in the cell cytoplasm as compared with the fluorescence resulted due to the irradiation using LED light. The $^1O_2$ ROS are produced in HeLa cancer cells under light irradiation. Therefore, all in vitro PDT results indicates the release of $^1O_2$ ROS by fBGn under irradiation of light. In further we quantitatively analyzed the PDT efficiency of fBGn and performed the cytotoxicity tests. As shown in **Figure 7h**, upon irradiation of laser light, a decrease in viability of HeLa cells with an increase in concentration of fBGn was seen, whereas significant PDT efficiency of fBGn can efficiently kill cancer cells owing to the presence of CDs inside the bioglass. The CDs produced sufficient $^1O_2$ ROS to effectively kill the cancer cells under 808nm light irradiation [22, 70, 72].

We studied the combined therapeutic effects of PDT/PTT on HeLa cancer cells with fBGn in vitro using a LIVE / DEAD assay (**Figure 7i**). This HeLa cells co-staining method with calcein-AM (green) and PI (red) can be used to differentiate live and dead cells respectively. In three groups (cell, fBGn, and irradiation light), no cell death was observed (absence of red fluorescence) because all the cells were live and showed green fluorescence. However, cells treated with fBGn showed auto-fluorescence of the fBGn in the cells without irradiation. This result showed that the cell media or water does not have the capability to generate $^1O_2$ ROS or heat under irradiation of light leading to cell death. HeLa cells were destroyed in presence of fBGn under 660 nm LED light (PDT) or 808 nm laser (PTT) because 660 nm light (PDT) and 808 nm laser (PTT) irradiation resulted in the formation of sufficient $^1O_2$ ROS or heat energy to effectively kill the cancer cells. However, by combining the PDT/PTT therapy, the rate of cell death decreased drastically when compared to the application of PDT and PTT separately. Whereas the intensity of red fluorescence significantly increased indicating the complete cell death. The combination of PDT/PTT of fBGn can effectively kill cancer cells under light irradiation.

We further quantitatively determined the PDT/PTT efficiency of fBGn from the Live/DEAD assay. As shown in **Figure 7j**, in vitro PDT/PTT, without fBGn with HeLa cells showed no reduction in cell viability under light irradiation. But it is observed that the cell viability of HeLa cells decreases when exposed to light of wavelength 660 nm light (PDT) or 808 nm laser (PTT). However, the combination of PDT/PTT, showed a significsnt reduction in cell viability as compared with the other treatment groups. Whereas enhanced efficiency of a combination of PDT/PTT in fBGn efficiently destroyed cancer cells by irradiating it under light irradiation. The maximum cell death observed indicates the higher therapeutic ability of fBGn in combination therapy.
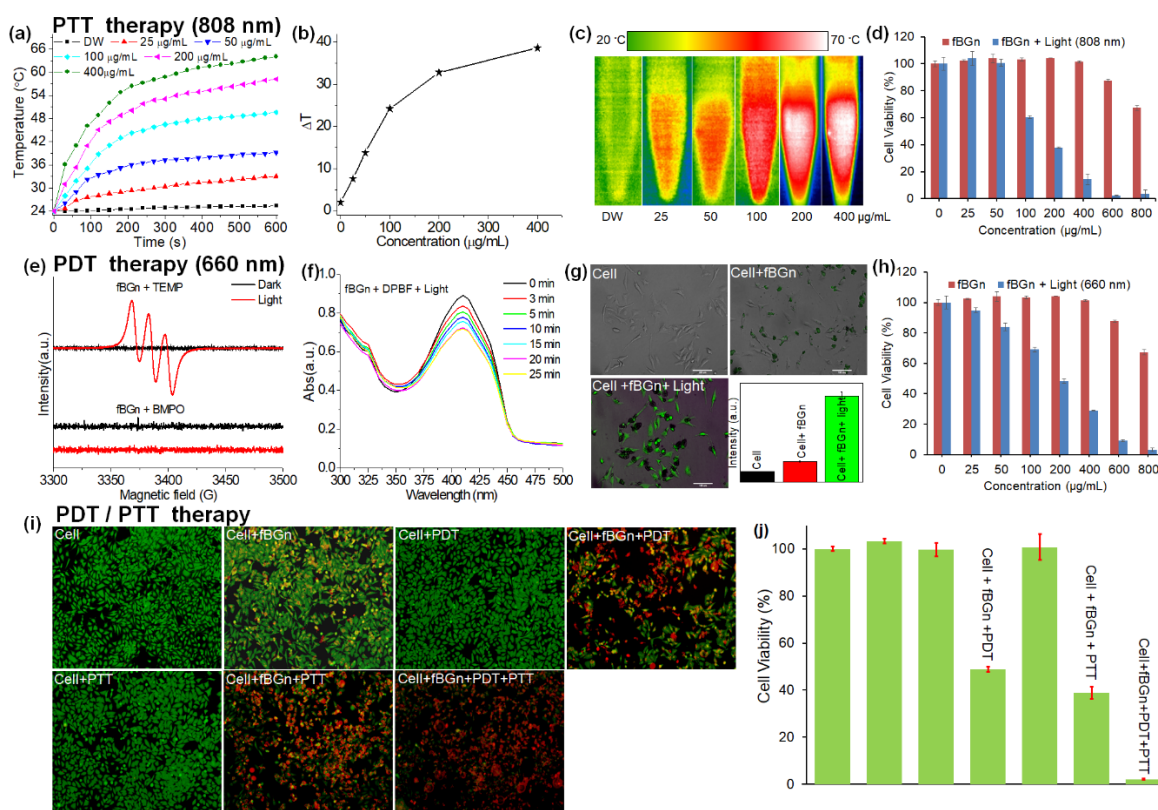

Figure 7. In vitro PDT/PTT therapy under light irradiation. In vitro results with PTT light (808 nm) with various concentrations of fBGn (a) Photothermal heating curves, (b) The changing temperature plot, (c) Temperature NIR images, and (d) Relative cell toxicity of HeLa cells. In vitro results with PDT light (80mW, 660 nm) with fBGn (e) a $^1O_2$ –induced signal of fBGn was examined by ESR spectra under dark and LED light conditions, (f) Photodegradation of DPBF, (g) ROS levels measured with HeLa cells treated with PBS, with fBGn, with fBGn + light irradiation, and the relative intensity, and (h) Cell toxicity of HeLa cells. In vitro imaging and combined PDT/PTT therapy under the light. (i) Confocal images of HeLa cells incubated with fBGn with various conditions and fluorescence images of calcien AM/PI-stained and (j) Cell toxicity of HeLa cells with various conditions.

3.6. Anticancer Drug Loading and Controlled Delivery for Chemotherapy

Another important method to destroy cancer cells is the efficient and targeted delivery of anticancer drugs in chemotherapy. The capacity to carry a drug into its target site without minimal loss of drug and structure of nanoparticles is an important requirement for developing effective mesoporous nanoparticles for specific site cargo delivery [48, 61, 73]. To attain this, fBGn with formed mesoporous structure was used for anticancer drug loading and controlled delivery. **Figure 8a** shows the drug loading efficiency of MSN and fBGn. The loading efficiency of fBGn was compared with MSN as a control, which has no Ca^{2+} ions inside the silica lattice. Mesoporous properties of MSN and fBGn were almost the same because of the similarities in their preparation methods. We have utilized it for the loading of anticancer drug DOX, which is positively charged and can interact electrostatically with the negative charge of fBGn. DOX was encapsulated inside the mesopores of fBGn. We have chosen three different concentrations of 80, 100, and 120 μg/mL. 1 mg of fBGn was added to each concentration for about 24h. We observed an increase in the loading amount with an increase in concentration. The loading efficiency of fBGn and MSN was ~ 92 % and ~ 67 %, respectively which indicates higher efficiency of fBGn as compared to MSN. The loading efficiency was significantly improved due to the Ca^{2+} ions (**Figure 8b**). The figure clearly shows higher drug loading and controlled release due to Ca^{2+} ions. DOX molecules exhibit two types of electrostatic interaction with Ca^{2+} ions and Si-OH groups. This is the main reason why fBGn have higher drug loading as compared to MSN without Ca^{2+} ions. Furthermore, we have studied the drug release from fBGn at pH (7.4 and 5.0) conditions. The environment of tumor cells are somewhat acidic with a pH ranging from 4.0-5.8 which indicates that the pH-dependent release is the chief factor for therapeutic delivery [45, 73, 74]. Nanoparticles were internalized into the endosomes and lysosomes in cancer cells which are slightly acidic with a pH 4.0-5.8. **Figure 8c** shows the drug release from fBGn and MSN under two different pH's for 48 h. MSN showed more drug release compared to fBGn under acidic conditions due to its strong bonding between Ca^{2+} ions and drug molecules. Drug molecules were first released under acidic conditions as compared to normal condition. This suggests that the fBGn has higher loading efficiency and controlled drug release property due to the effect of Ca^{2+} ions which can be used for cancer chemotherapy. We further studied the delivery of drug molecules into the HeLa cells by cytotoxicity tests using CCK-8 assay. HeLa cells were treated with different concentrations of fBGn, DOX, and fBGn-DOX for 24 h. As shown in **Figure**

8d, the fBGn concentration up to 320 µg/mL showed no significant cell toxicity effects on HeLa cells. Free DOX indicates slightly lower cell toxicity as compared to fBGn-DOX at concentrations ranging from 5 to 40 µg/mL. In the first 24 h, the drug release of fBGn-DOX was not enough to destroy the cells at any specific concentration. On the contrary, the concentration of fBGn-DOX (80–640 µg/mL) showed higher cell viability as compared to free DOX which indicates that the fBGn-DOX drug release was enough to destroy the cancer cells. This controlled release based on fBGn can be utilized in the near future for cancer chemotherapy.
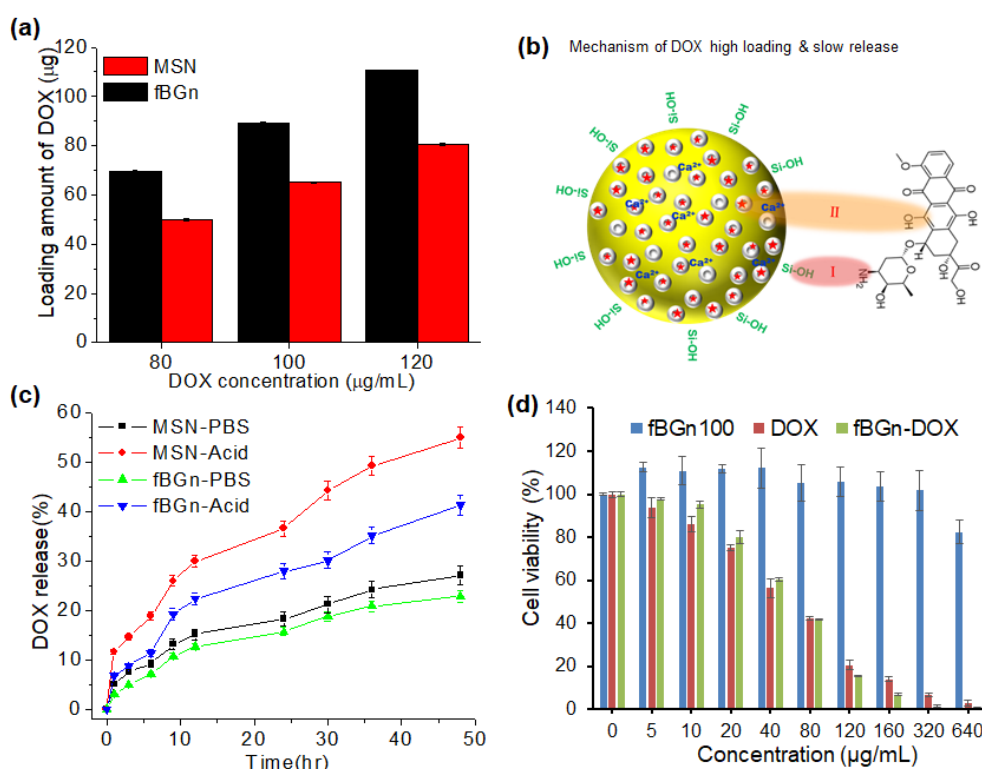

Figure 8. Anticancer drug DOX loading and release study using fBGn and MSN. (a) Anticancer drug loading, (b) loading and release mechanism. (c) DOX release at pH (5.0 and 7.4) at 37 °C. (d) Cell viability of HeLa cells.

3.7. In-vivo Imaging and Biocompatibility

Fluorescence imaging is one of the most important requirements for observation and real-time imaging during the diagnosis of cancer sites. fBGn was dispersed in a saline solution and is used for in vivo imaging in a nude mouse model. First, we observed that the emission images of fBGn under the corresponding excitation wavelength as shown in **Figure S7a**. This suggests that fBGn has multicolour fluorescence. We have detected the fluorescence image in nude mouse with a local injection of fBGn

(**Figure S7b)**. It can be concluded that fBGn possess excellent properties for real-time imaging and phototherapy which can be utilized for effective cancer treatment.

In-vivo compatibility was used to determine the clinical potential of fBGn nanoparticles. The in-vivo biocompatibility studies of fBGn using varying doses (0, 5, 10, and 20 mg/kg) was evaluated by IV injection into a nude mouse. After 2 weeks, the rat was sacrificed and the tissues from major organs was collected. The biocompatibility was then analyzed using H&E staining **Figure S8**. The fBGn with varying doses showed no significant difference in the tissued compared to saline control group. The fBGn nanoparticles present in almost all the organs showed high histocompatibility.

Systematic **scheme 1c** shows that fBGn can be utilized for various biomedical applications such as real-time theranostic applications in fluorescence imaging, Raman imaging, two-photon fluorescence imaging, controlled drug delivery, combined photothermal and photodynamic synergistic cancer therapy. Phototherapy with multimodal imaging is a promising strategy in the medical field which can significantly improve the quality of tumor therapy owing to its benefits such as real-time observation of cancer sites and light-induced destruction of cancer cells. In the future, we are planning to design an extensive study on fBGn by modifying it by PEGylation and applying it for cancer cell targeting in 'systemic' tumor theranostics. This in vivo design involves extensive work as a follow-up study for the current nanoparticle system.

4. CONCLUSIONS

Multi-color fluorescent fBGn were developed for cancer theranostics through a direct and label-free approach. The calcination at 400 °C provided fBGn with high fluorescence intensity that origined from the CD. The fBGn showed triple-mode emission (FI, TP, and RI) and phototherapeutic effects (PTT and PDT) on cancer cells. Furthermore, fBGn were effective in delivering DOX in a pH-dependent manner. The multifunctional fBGn (anticancer delivery, multi-bioimaging, and combined PTT and PDT therapy) are considered as an exciting nanoplatform for cancer theranostics.

ASSOCIATED CONTENT

Supporting Information. The Supporting Information includes Figures S1-S8 (Mesoporous curve, multi-peaks fitting, area of three peaks, PL emission photographs, Photothermal efficiency, rate of

singlet oxygen generation, In-vivo imaging and biocompatibility).

AUTHOR INFORMATION

Corresponding Author

*singhiitgphd@gmail.com; *kimhw@dku.edu

Author Contributions

All authors have given approval to the final version of the manuscript.

REFERENCES

(1) Cheng, L.; Wang, C.; Feng, L.; Yang, K.; Liu, Z., Functional Nanomaterials for Phototherapies of Cancer. *Chem. Rev.* **2014,** *114*, 10869-10939.

(2) Lin, J.; Wang, M.; Hu, H.; Yang, X.; Wen, B.; Wang, Z.; Jacobson, O.; Song, J.; Zhang, G.; Niu, G.; Huang, P.; Chen, X., Multimodal-Imaging-Guided Cancer Phototherapy by Versatile Biomimetic Theranostics with Uv and Γ-Irradiation Protection. *Adv. Mater.* **2016,** *28*, 3273-3279.

(3) Wang, C.; Fan, W.; Zhang, Z.; Wen, Y.; Xiong, L.; Chen, X., Advanced Nanotechnology Leading the Way to Multimodal Imaging-Guided Precision Surgical Therapy. *Adv. Mater.* **2019,** *31*, 1904329.

(4) Shi, H.; Sun, Y.; Yan, R.; Liu, S.; Zhu, L.; Liu, S.; Feng, Y.; Wang, P.; He, J.; Zhou, Z.; Ye, D., Magnetic Semiconductor Gd-Doping Cus Nanoparticles as Activatable Nanoprobes for Bimodal Imaging and Targeted Photothermal Therapy of Gastric Tumors. *Nano Lett.* **2019,** *19*, 937-947.

(5) Gao, M.; Yu, F.; Lv, C.; Choo, J.; Chen, L., Fluorescent Chemical Probes for Accurate Tumor Diagnosis and Targeting Therapy. *Chem. Soc. Rev.* **2017,** *46*, 2237-2271.

(6) Dolmans, D. E. J. G. J.; Fukumura, D.; Jain, R. K., Photodynamic Therapy for Cancer. *Nat. Rev. Cancer* **2003,** *3*, 380-387.

(7) Celli, J. P.; Spring, B. Q.; Rizvi, I.; Evans, C. L.; Samkoe, K. S.; Verma, S.; Pogue, B. W.; Hasan, T., Imaging and Photodynamic Therapy: Mechanisms, Monitoring, and Optimization. *Chem. Rev.* **2010,** *110*, 2795-2838.

(8) Xu, M.; Yang, G.; Bi, H.; Xu, J.; Feng, L.; Yang, D.; Sun, Q.; Gai, S.; He, F.; Dai, Y.; Zhong, C.; Yang, P., Combination of CuS and G-C$_3$N$_4$ Qds on Upconversion Nanoparticles for Targeted Photothermal and Photodynamic Cancer Therapy. *Chem. Eng. J.* **2019,** 360, 866-878.

(9) Jung, H. S.; Han, J.; Shi, H.; Koo, S.; Singh, H.; Kim, H.-J.; Sessler, J. L.; Lee, J. Y.; Kim, J.-H.; Kim, J. S., Overcoming the Limits of Hypoxia in Photodynamic Therapy: A Carbonic Anhydrase Ix-Targeted Approach. *J. Am. Chem. Soc.* **2017,** *139*, 7595-7602.

(10) Imberti, C.; Zhang, P.; Huang, H.; Sadler, P. J., New Designs for Phototherapeutic Transition Metal Complexes. *Angew. Chem. Int. Ed.* **2020,** *59*, 61-73.

(11) Gai, S.; Yang, G.; Yang, P.; He, F.; Lin, J.; Jin, D.; Xing, B., Recent Advances in Functional Nanomaterials for Light–Triggered Cancer Therapy. *Nano Today* **2018,** 19, 146-187.

(12) Lucky, S. S.; Soo, K. C.; Zhang, Y., Nanoparticles in Photodynamic Therapy. *Chem. Rev.* **2015,** *115*, 1990-2042.

(13) Zhang, X.; Xi, Z.; Machuki, J. O. a.; Luo, J.; Yang, D.; Li, J.; Cai, W.; Yang, Y.; Zhang, L.; Tian, J.; Guo, K.; Yu, Y.; Gao, F., Gold Cube-in-Cube Based Oxygen Nanogenerator: A Theranostic Nanoplatform for Modulating Tumor Microenvironment for Precise Chemo-Phototherapy and Multimodal Imaging. *ACS Nano* **2019,** *13*, 5306-5325.

(14) Vankayala, R.; Hwang, K. C., Near-Infrared-Light-Activatable Nanomaterial-Mediated Phototheranostic Nanomedicines: An Emerging Paradigm for Cancer Treatment. *Adv. Mater.* **2018,** *30*, 1706320.

(15) Nam, J.; Son, S.; Ochyl, L. J.; Kuai, R.; Schwendeman, A.; Moon, J. J., Chemo-Photothermal Therapy Combination Elicits Anti-Tumor Immunity against Advanced Metastatic Cancer. *Nat. Commun.* **2018,** *9*, 1074.

(16) Alifu, N.; Zebibula, A.; Qi, J.; Zhang, H.; Sun, C.; Yu, X.; Xue, D.; Lam, J. W. Y.; Li, G.; Qian, J.; Tang, B. Z., Single-Molecular near-Infrared-Ii Theranostic Systems: Ultrastable Aggregation-Induced Emission Nanoparticles for Long-Term Tracing and Efficient Photothermal Therapy. *ACS Nano* **2018,** *12*, 11282-11293.

(17) Jang, B.; Park, J.-Y.; Tung, C.-H.; Kim, I.-H.; Choi, Y., Gold Nanorod−Photosensitizer Complex for near-Infrared Fluorescence Imaging and Photodynamic/Photothermal Therapy in Vivo. *ACS Nano* **2011,** *5*, 1086-1094.

(18) Dong, S.; Xu, J.; Jia, T.; Xu, M.; Zhong, C.; Yang, G.; Li, J.; Yang, D.; He, F.; Gai, S.; Yang, P.; Lin, J., Upconversion-Mediated Znfe2o4 Nanoplatform for Nir-Enhanced Chemodynamic and Photodynamic Therapy. *Chem. Sci.* **2019,** 10, (15), 4259-4271.

(19) Panwar, N.; Soehartono, A. M.; Chan, K. K.; Zeng, S.; Xu, G.; Qu, J.; Coquet, P.; Yong, K.-T.; Chen, X., Nanocarbons for Biology and Medicine: Sensing, Imaging, and Drug Delivery. *Chem. Rev.* **2019,** *119*, 9559-9656.

(20) Saleem, J.; Wang, L.; Chen, C., Carbon-Based Nanomaterials for Cancer Therapy Via Targeting Tumor Microenvironment. *Adv. Healthc. Mater.* **2018,** *7*, 1800525.

(21) Patel, K. D.; Singh, R. K.; Kim, H.-W., Carbon-Based Nanomaterials as an Emerging Platform for Theranostics. *Mater. Horizons* **2019,** *6*, 434-469.

(22) Ge, J.; Jia, Q.; Liu, W.; Lan, M.; Zhou, B.; Guo, L.; Zhou, H.; Zhang, H.; Wang, Y.; Gu, Y.; Meng, X.; Wang, P., Carbon Dots with Intrinsic Theranostic Properties for Bioimaging, Red-Light-Triggered Photodynamic/Photothermal Simultaneous Therapy in Vitro and in Vivo. *Adv. Healthc. Mater.* **2016,** *5*, 665-675.

(23) McCarthy, J. R.; Weissleder, R., Multifunctional Magnetic Nanoparticles for Targeted Imaging and Therapy. *Adv. Drug Deliv. Rev.* **2008,** *60*, 1241-1251.

(24) Shen, Z.; Chen, T.; Ma, X.; Ren, W.; Zhou, Z.; Zhu, G.; Zhang, A.; Liu, Y.; Song, J.; Li, Z.; Ruan, H.; Fan, W.; Lin, L.; Munasinghe, J.; Chen, X.; Wu, A., Multifunctional Theranostic Nanoparticles Based on Exceedingly Small Magnetic Iron Oxide Nanoparticles for T1-Weighted Magnetic Resonance Imaging and Chemotherapy. *ACS Nano* **2017,** *11*, 10992-11004.

(25) Kim, D.; Shin, K.; Kwon, S. G.; Hyeon, T., Synthesis and Biomedical Applications of Multifunctional Nanoparticles. *Adv. Mater.* **2018,** *30*, 1802309.

(26) He, F.; Yang, G.; Yang, P.; Yu, Y.; Lv, R.; Li, C.; Dai, Y.; Gai, S.; Lin, J., A New Single 808 Nm Nir Light-Induced Imaging-Guided Multifunctional Cancer Therapy Platform. *Adv. Functional Mater.* **2015,** *25, (25)*, 3966-3976.

(27) Samia, A. C. S.; Chen, X.; Burda, C., Semiconductor Quantum Dots for Photodynamic Therapy. *J. Am. Chem.*

Soc. **2003,** *125*, 15736-15737.

(28) Cao, L.; Wang, X.; Meziani, M. J.; Lu, F.; Wang, H.; Luo, P. G.; Lin, Y.; Harruff, B. A.; Veca, L. M.; Murray, D.; Xie, S.-Y.; Sun, Y.-P., Carbon Dots for Multiphoton Bioimaging. *J. Am. Chem. Soc.* **2007,** *129*, 11318-11319.

(29) Hong, G.; Diao, S.; Antaris, A. L.; Dai, H., Carbon Nanomaterials for Biological Imaging and Nanomedicinal Therapy. *Chem. Rev.* **2015,** *115*, 10816-10906.

(30) Khan, S.; Gupta, A.; Verma, N. C.; Nandi, C. K., Time-Resolved Emission Reveals Ensemble of Emissive States as the Origin of Multicolor Fluorescence in Carbon Dots. *Nano Lett.* **2015,** *15*, 8300-8305.

(31) Molaei, M. J., Carbon Quantum Dots and Their Biomedical and Therapeutic Applications: A Review. *RSC Adv.* **2019,** *9*, 6460-6481.

(32) Liu, M. L.; Chen, B. B.; Li, C. M.; Huang, C. Z., Carbon Dots: Synthesis, Formation Mechanism, Fluorescence Origin and Sensing Applications. *Green Chem.* **2019,** *21*, 449-471.

(33) Zuo, P.; Lu, X.; Sun, Z.; Guo, Y.; He, H., A Review on Syntheses, Properties, Characterization and Bioanalytical Applications of Fluorescent Carbon Dots. *Microchimica Acta* **2016,** *183*, 519-542.

(34) Kim, H. M.; Cho, B. R., Small-Molecule Two-Photon Probes for Bioimaging Applications. *Chem. Rev.* **2015,** *115*, 5014-5055.

(35) Lim, C. S.; Cho, B. R., Two-Photon Probes for Biomedical Applications. *BMB Rep.* **2013,** *46*, 188-194.

(36) Meng, H.-M.; Zhao, D.; Li, N.; Chang, J., A Graphene Quantum Dot-Based Multifunctional Two-Photon Nanoprobe for the Detection and Imaging of Intracellular Glutathione and Enhanced Photodynamic Therapy. *Analyst* **2018,** *143*, 4967-4973.

(37) Feng, L.-L.; Wu, Y.-X.; Zhang, D.-L.; Hu, X.-X.; Zhang, J.; Wang, P.; Song, Z.-L.; Zhang, X.-B.; Tan, W., Near Infrared Graphene Quantum Dots-Based Two-Photon Nanoprobe for Direct Bioimaging of Endogenous Ascorbic Acid in Living Cells. *Anal. Chem.* **2017,** *89*, 4077-4084.

(38) Tang, J.; Kong, B.; Wu, H.; Xu, M.; Wang, Y.; Wang, Y.; Zhao, D.; Zheng, G., Carbon Nanodots Featuring Efficient Fret for Real-Time Monitoring of Drug Delivery and Two-Photon Imaging. *Adv. Mater.* **2013,** *25*, 6569-6574.

(39) Liu, Z.; Li, S.; Xia, X.; Zhu, Z.; Chen, L.; Chen, Z., Recent Advances in Multifunctional Graphitic Nanocapsules for Raman Detection, Imaging, and Therapy. *Small Methods* **2019,** 1900440, 1-26.

(40) Zhou, H.; Zou, F.; Tran, V. T.; Lee, J., Simultaneous Enhancement of Raman Scattering and Fluorescence Emission on Graphene Quantum Dot-Spiky Magnetoplasmonic Supra-Particle Composite Films. *RSC Adv.* **2015,** *5*, 81753-81758.

(41) Bartelmess, J.; Quinn, S. J.; Giordani, S., Carbon Nanomaterials: Multi-Functional Agents for Biomedical Fluorescence and Raman Imaging. *Chem. Soc. Rev.* **2015,** *44*, 4672-4698.

(42) Zhang, Y.; Wu, M.; Wu, M.; Zhu, J.; Zhang, X., Multifunctional Carbon-Based Nanomaterials: Applications in Biomolecular Imaging and Therapy. *ACS omega* **2018,** *3*, 9126-9145.

(43) Ding, Y.; Du, C.; Qian, J.; Dong, C.-M., Nir-Responsive Polypeptide Nanocomposite Generates No Gas, Mild Photothermia, and Chemotherapy to Reverse Multidrug-Resistant Cancer. *Nano Lett.* **2019,** *19*, 4362-4370.

(44) Kwon, S.; Singh, R. K.; Perez, R. A.; Abou Neel, E. A.; Kim, H.-W.; Chrzanowski, W., Silica-Based Mesoporous Nanoparticles for Controlled Drug Delivery. *J. Tissue Eng.* **2013,** *4*, 1-18.

(45) Baek, S.; Singh, R. K.; Khanal, D.; Patel, K. D.; Lee, E.-J.; Leong, K. W.; Chrzanowski, W.; Kim, H.-W., Smart Multifunctional Drug Delivery Towards Anticancer Therapy Harmonized in Mesoporous Nanoparticles. *Nanoscale* **2015,** *7*, 14191-14216.

(46) Owens, G. J.; Singh, R. K.; Foroutan, F.; Alqaysi, M.; Han, C.-M.; Mahapatra, C.; Kim, H.-W.; Knowles, J. C., Sol–Gel Based Materials for Biomedical Applications. *Prog. Mater. Sci.* **2016,** *77*, 1-79.

(47) Singh, R. K.; Patel, K. D.; Mahapatra, C.; Kang, M. S.; Kim, H.-W., C-Dot Generated Bioactive Organosilica Nanospheres in Theranostics: Multicolor Luminescent and Photothermal Properties Combined with Drug Delivery Capacity. *ACS Appl. Mater. Interfaces* **2016,** *8*, 24433-24444.

(48) Singh, R. K.; Patel, K. D.; Leong, K. W.; Kim, H.-W., Progress in Nanotheranostics Based on Mesoporous Silica Nanomaterial Platforms. *ACS Appl. Mater. Interfaces* **2017,** *9*, 10309-10337.

(49) Perez, R. A.; Singh, R. K.; Kim, T.-H.; Kim, H.-W., Silica-Based Multifunctional Nanodelivery Systems toward Regenerative Medicine. *Mater. Horiz.* **2017,** *4*, 772-799.

(50) Kim, T.-H.; Singh, R. K.; Kang, M. S.; Kim, J.-H.; Kim, H.-W., Gene Delivery Nanocarriers of Bioactive Glass with Unique Potential to Load Bmp2 Plasmid DNA and to Internalize into Mesenchymal Stem Cells for Osteogenesis and Bone Regeneration. *Nanoscale* **2016,** *8*, 8300-8311.

(51) Patel, K. D.; Buitrago, J. O.; Parthiban, S. P.; Lee, J.-H.; Singh, R. K.; Knowles, J. C.; Kim, H.-W., Combined Effects of Nanoroughness and Ions Produced by Electrodeposition of Mesoporous Bioglass Nanoparticle for Bone Regeneration. *ACS Appl. Bio Mater.* **2019,** 2, (11), 5190-5203.

(52) Kang, M. S.; Lee, N.-H.; Singh, R. K.; Mandakhbayar, N.; Perez, R. A.; Lee, J.-H.; Kim, H.-W., Nanocements Produced from Mesoporous Bioactive Glass Nanoparticles. *Biomaterials* **2018,** *162*, 183-199.

(53) Bao, X.; Yuan, Y.; Chen, J.; Zhang, B.; Li, D.; Zhou, D.; Jing, P.; Xu, G.; Wang, Y.; Holá, K.; Shen, D.; Wu, C.; Song, L.; Liu, C.; Zbořil, R.; Qu, S., In Vivo Theranostics with near-Infrared-Emitting Carbon Dots—Highly Efficient Photothermal Therapy Based on Passive Targeting after Intravenous Administration. *Light: Science & Applications* **2018,** *7*, 91.

(54) Tian, Q.; Jiang, F.; Zou, R.; Liu, Q.; Chen, Z.; Zhu, M.; Yang, S.; Wang, J.; Wang, J.; Hu, J., Hydrophilic Cu9s5 Nanocrystals: A Photothermal Agent with a 25.7% Heat Conversion Efficiency for Photothermal Ablation of Cancer Cells in Vivo. *ACS Nano* **2011,** *5*, 9761-9771.

(55) Roy, P.; Chen, P.-C.; Periasamy, A. P.; Chen, Y.-N.; Chang, H.-T., Photoluminescent Carbon Nanodots: Synthesis, Physicochemical Properties and Analytical Applications. *Mater. Today* **2015,** *18*, 447-458.

(56) Pan, D.; Zhang, J.; Li, Z.; Wu, M., Hydrothermal Route for Cutting Graphene Sheets into Blue-Luminescent Graphene Quantum Dots. *Adv. Mater.* **2010,** *22*, 734-738.

(57) Wu, J.-B.; Lin, M.-L.; Cong, X.; Liu, H.-N.; Tan, P.-H., Raman Spectroscopy of Graphene-Based Materials and Its Applications in Related Devices. *Chem. Soc. Rev.* **2018,** *47*, 1822-1873.

(58) Muangrat, W.; Wongwiriyapan, W.; Morimoto, S.; Hashimoto, Y., Graphene Nanosheet-Grafted Double-Walled Carbon Nanotube Hybrid Nanostructures by Two-Step Chemical Vapor Deposition and Their Application for Ethanol Detection. *Sci. Rep.* **2019,** *9*, 7871.

(59) Ding, H.; Yu, S.-B.; Wei, J.-S.; Xiong, H.-M., Full-Color Light-Emitting Carbon Dots with a Surface-State-Controlled Luminescence Mechanism. *ACS Nano* **2016,** *10*, 484-491.

(60) Singh, R. K.; Kim, T.-H.; Mahapatra, C.; Patel, K. D.; Kim, H.-W., Preparation of Self-Activated Fluorescence Mesoporous Silica Hollow Nanoellipsoids for Theranostics. *Langmuir* **2015,** *31*, 11344-11352.

(61) Kwon, S.; Singh, R. K.; Kim, T.-H.; Patel, K. D.; Kim, J.-J.; Chrzanowski, W.; Kim, H.-W., Luminescent Mesoporous Nanoreservoirs for the Effective Loading and Intracellular Delivery of Therapeutic Drugs. *Acta Biomaterialia* **2014,** *10*, 1431-1442.

(62) Zhu, S.; Zhang, J.; Tang, S.; Qiao, C.; Wang, L.; Wang, H.; Liu, X.; Li, B.; Li, Y.; Yu, W.; Wang, X.; Sun, H.; Yang, B., Surface Chemistry Routes to Modulate the Photoluminescence of Graphene Quantum Dots: From Fluorescence Mechanism to up-Conversion Bioimaging Applications. *Adv. Funct. Mater.* **2012,** *22*, 4732-4740.

(63) Zhang, Q.; Deng, S.; Liu, J.; Zhong, X.; He, J.; Chen, X.; Feng, B.; Chen, Y.; Ostrikov, K., Cancer-Targeting Graphene Quantum Dots: Fluorescence Quantum Yields, Stability, and Cell Selectivity. *Adv. Funct. Mater.*

2019, *29*, 1805860.

(64) Miller, D. R.; Jarrett, J. W.; Hassan, A. M.; Dunn, A. K., Deep Tissue Imaging with Multiphoton Fluorescence Microscopy. *Curr. Opin. Biomed. Eng.* **2017,** *4*, 32-39.

(65) Shen, Y.; Shuhendler, A. J.; Ye, D.; Xu, J.-J.; Chen, H.-Y., Two-Photon Excitation Nanoparticles for Photodynamic Therapy. *Chem. Soc. Rev.* **2016,** *45*, 6725-6741.

(66) Yao, S.; Belfield, K. D., Two-Photon Fluorescent Probes for Bioimaging. *Euro. J. Org. Chem.* **2012,** 2012, (17), 3199-3217.

(67) Zhang, Z.; Liu, Q.; Gao, D.; Luo, D.; Niu, Y.; Yang, J.; Li, Y., Graphene Oxide as a Multifunctional Platform for Raman and Fluorescence Imaging of Cells. *Small* **2015,** *11*, 3000-3005.

(68) Ma, X.; Qu, Q.; Zhao, Y.; Luo, Z.; Zhao, Y.; Ng, K. W.; Zhao, Y., Graphene Oxide Wrapped Gold Nanoparticles for Intracellular Raman Imaging and Drug Delivery. *J. Mater. Chem. B* **2013,** *1*, 6495-6500.

(69) Ge, J.; Jia, Q.; Liu, W.; Lan, M.; Zhou, B.; Guo, L.; Zhou, H.; Zhang, H.; Wang, Y.; Gu, Y.; Meng, X.; Wang, P., Carbon Dots with Intrinsic Theranostic Properties for Bioimaging, Red-Light-Triggered Photodynamic/Photothermal Simultaneous Therapy in Vitro and in Vivo. *Adv. Healthc. Mater.* **2016,** *5*, 665-675.

(70) Lan, M.; Guo, L.; Zhao, S.; Zhang, Z.; Jia, Q.; Yan, L.; Xia, J.; Zhang, H.; Wang, P.; Zhang, W., Carbon Dots as Multifunctional Phototheranostic Agents for Photoacoustic/Fluorescence Imaging and Photothermal/Photodynamic Synergistic Cancer Therapy. *Adv. Therap.* **2018,** *1*, 1800077.

(71) Pan, D.; Zhong, X.; Zhao, W.; Yu, Z.; Yang, Z.; Wang, D.; Cao, H.; He, W., Meso-Substituted Porphyrin Photosensitizers with Enhanced near-Infrared Absorption: Synthesis, Characterization and Biological Evaluation for Photodynamic Therapy. *Tetrahedron* **2018,** 74, (21), 2677-2683.

(72) Jijie, R.; Barras, A.; Bouckaert, J.; Dumitrascu, N.; Szunerits, S.; Boukherroub, R., Enhanced Antibacterial Activity of Carbon Dots Functionalized with Ampicillin Combined with Visible Light Triggered Photodynamic Effects. *Colloids Surf. B Biointerfaces* **2018,** 170, 347-354.

(73) Kang, M. S.; Singh, R. K.; Kim, T.-H.; Kim, J.-H.; Patel, K. D.; Kim, H.-W., Optical Imaging and Anticancer Chemotherapy through Carbon Dot Created Hollow Mesoporous Silica Nanoparticles. *Acta Biomater.* **2017,** *55*, 466-480.

(74) Baek, S.; Singh, R. K.; Kim, T.-H.; Seo, J.-w.; Shin, U. S.; Chrzanowski, W.; Kim, H.-W., Triple Hit with Drug Carriers: Ph- and Temperature-Responsive Theranostics for Multimodal Chemo- and Photothermal Therapy and Diagnostic Applications. *ACS Appl. Mater. Interfaces* **2016,** *8*, 8967-8979.

Graphical TOC